



Contents lists available at SciVerse ScienceDirect

Journal of Structural Biology

journal homepage: www.elsevier.com/locate/yjsbi

Assessing the benefits of focal pair cryo-electron tomography

Mikhail Kudryashev, Henning Stahlberg*, Daniel Castaño-Díez*

Center for Cellular Imaging and NanoAnalytics (C-CINA), Biozentrum, University Basel, WRO-1058, Mattenstrasse 26, CH-4058 Basel, Switzerland

ARTICLE INFO

Article history:

Available online xxx

Keywords:

Cryo electron tomography
Image processing
CTF correction

ABSTRACT

Cryo electron tomography provides nanometer-scale information on biological matter preserved in a close-to native state. The resolution of tomograms and structures resolved by sub-tomogram averaging is typically limited by the contrast transfer function of the electron microscope, which is especially critical for thick samples. Here, we report a method to increase the attainable resolution by recording tomographic ‘focal pairs’, which are pairs of tilt series of the same object acquired in complementary defocus conditions. Low defocus imaging provides high resolution at low contrast, while high defocus imaging yields high contrast at the price of limited resolution. Quantitative assessment of the quality of lipid bilayer reconstructions in the resulting tomograms demonstrates stable resolution preservation beyond 3 nm for cells thicker than 500 nm. Further, in computational simulations on synthetic datasets we show the applicability of the method to sub-tomogram averaging, demonstrating its potential for achieving higher resolution.

© 2011 Elsevier Inc. All rights reserved.

1. Introduction

Cryo electron tomography (cryo-ET) is a powerful tool for the study of macromolecular architecture of cells in close-to-native preservation at nanometer scale (Leis et al., 2008). This technique has three primary fields of applications: for cellular biology, it bridges the gap between light microscopy and higher resolution structures and allows whole cell imaging at macromolecular scale (Patla et al., 2010; Urban et al., 2010). For structural biology, cryo-ET with sub-tomogram averaging combines preservation of the macromolecule in the context of the cell with three-dimensionality of every separate macromolecule, allowing the exploration of flexibility and heterogeneity of the object (Beck et al., 2007; Liu et al., 2008; Ortiz et al., 2010). For systems biology, cryo-ET may contribute spatial localization of macromolecules inside a cell such as their distribution and mutual orientation (Beck et al., 2009; Brandt et al., 2010). This is implemented using template matching, a procedure closely related to sub-tomogram alignment from an operational point of view.

Structures determined by sub-tomogram averaging from cryo-ET in the past typically reached a resolution of 2–8 nm depending on the thickness of the observed sample, with 2–4 nm for small viruses (Briggs et al., 2009; Liu et al., 2008) and thin bacteria like spirochetes (Liu et al., 2009). Most tomographic reconstructions for thicker objects (limited by ~500 nm) have a resolution worse than 5 nm, reducing the applicability of cryo-ET in such samples

to very large macromolecules and macromolecular ensembles. Additional factors limiting resolution of structures solved from cryo-ET include heterogeneity of objects (Beck et al., 2007), corrupted mutual alignment of particles (Amat et al., 2010a), insufficient particle statistics, and limiting imaging conditions at the microscopy level.

The resolution of a tomographic reconstruction can be defined as that frequency, at which the resolution-dependent signal-to-noise ratio (SNR) is still above a defined value (Grigorieff, 2000). The interpretable resolution of a tomogram can be improved by sub-volume averaging, whereby multiple sub-volumes with the same type of macromolecules are aligned and averaged. The resulting average structure then shows a better SNR at higher resolutions. Pre-requisite for such alignment is, however, that the structural details in the sub-volumes can be recognized for proper alignment. The recent arrival of first direct electron detection devices (Faruqi and McMullan, 2011) to replace charge-coupled cameras (CCD) or photographic film in the electron microscopes is likely to extend the attainable resolution in electron tomography in the near future. Nevertheless, even with such cameras, the problem of a SNR-limited resolution of cryo-ET and its dependence on the contrast of the instrument remains unchanged.

In this context and as pointed out by others before (e.g. John Briggs, personal communication) it is also interesting to note that the so-called Crowther Criterion (Crowther and Klug, 1971) that defines a resolution limit in electron tomography datasets as a function of the sample thickness and the tilt angle increments does not apply for reconstructions after tomographic sub-volume averaging: The averaged reconstruction originating from several differently oriented sub-volumes comprises data in finely sampled

* Corresponding authors. Fax: +41 61 387 39 86 (H. Stahlberg).

E-mail addresses: Henning.Stahlberg@unibas.ch (H. Stahlberg), Daniel.Castano-Diez@unibas.ch (D. Castaño-Díez).

angle increments. This allows tomographic data collection to be done with fewer images at much coarser tilt angle increments, so that each individual image frame can benefit from a higher SNR. As a consequence, data collection in tilt-pair random conical tilt geometry can therefore be interpreted as tomographic data collection with a strongly increased tilt angle increment.

Contrast in cryo-electron microscopy (cryo-EM) is mainly formed by phase contrast from elastically scattered electrons that interfere with non-scattered (i.e. elastically forward scattered) electrons in the image plane. In addition, inelastically scattered electrons contribute absorption contrast to the image, or they add a diffuse scattering background to the noise level in the image. Inelastically scattered electrons are mostly forward scattered, so that their content transfer at high-resolution falls off rapidly (Wade, 1992). In cryo-EM in the absence of a phase plate device (Nagayama and Danev, 2008), the phase contrast in recorded images is improved by defocusing the microscope's objective lens. The amount of defocusing modulates the balance between resolution and contrast of the micrograph. This balance is quantitatively described by the contrast transfer function (CTF, Scherzer, 1948), where the phase-contrast transfer is described by a sinusoidal function that modulates the frequency components of the projected EM image (Fig. 1A). This oscillating function is further modulated by an envelope function, which degrades the high-resolution information. Both, the oscillation frequency as also the envelope function strongly depend on the employed defocus value of the microscope's objective lens. Higher defocus values result in a CTF with higher contrast at low resolution, faster oscillations towards higher resolution, and a more rapid decay of the contrast transfer towards higher resolution from the dampening of the envelope due to the limited spatial coherence in the illumination.

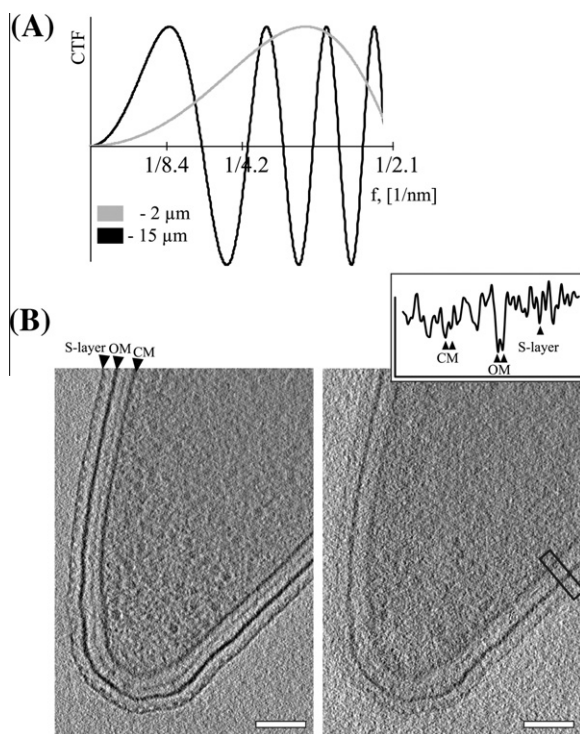


Fig. 1. High- and low-defocus tomograms. (A) Simulated CTF of a 300 keV electron microscope for high (15 μm , black) and low (2 μm , gray) defocus with a pixel size of 1.05 nm. (B) 20 nm thick sections through tomograms of *Caulobacter crescentus* at high-defocus (right) aligned by fiducial gold markers and low-defocus (left) aligned to high-defocus tilt series with global alignment ('Method 1'). Inset: electron density profile of a lateral projection of the membrane cross-section indicated by the black box. Arrowheads point to cytoplasmic membrane (CM), outer membrane (OM) and S-layer. Scale bars: 100 nm.

A zero value of the CTF implies a complete loss of information at that resolution.

For electron tomography datasets of biological specimens thicker than 500 nm that are recorded at intermediate voltages (200...300 kV) typically a defocus setting of 10–18 μm is employed that places the first zero of the CTF at around 4–7 nm^{-1} (Beck et al., 2007; Chen et al., 2011; Ortiz et al., 2010), a value that correlates with the declared resolution in the majority of the published tomography structures in the past.

CTF determination and CTF correction of image data commonly applied in single particle cryo-EM (Frank, 2009) encounters three major problems with images from tomographic tilt series. First, the electron dose that would be used for one micrograph in a single particle image is distributed over the tilt series, which significantly reduces the signal to noise ratio in one individual image, thus complicating the determination of the CTF for a single image. Second – the sample is tilted, this generates a defocus gradient within the image, for which a clear CTF correction is not straightforward (Henderson et al., 1990; Philippsen et al., 2007). Thirdly, in thick samples the recorded image is in a first approximation a superposition of projection images from different layers of the sample, each recorded with a different defocus value and thereby convoluted with a different CTF.

Several algorithms and software implementations are available for CTF determination and for CTF correction in cryo-EM images; correction for nominal defocus in electron tomograms has been implemented (Fernandez et al., 2006; Winkler, 2007). More recent approaches are aimed at determining CTF parameters from tilt series; this has been applied for samples embedded in thin ice layers (Xiong et al., 2009) and relatively small virus particles (Zanetti et al., 2009). Using the latter approach, Briggs and colleagues improved resolution of Gag, a major structural protein of HIV from 21 to 17 Å, extending the reconstructed resolution beyond the first towards the second zero (Thon ring, Thon, 1971) of the CTF (Briggs et al., 2009). CTF correction applied to images of the 70S ribosome from intact *Escherichia coli* cells allowed better resemblance of the resulting reconstruction to the structure determined by X-ray crystallography, especially in the frequency range between the first and second zeros of CTF (Ortiz et al., 2010), this however did not increase the resolution significantly above the resolution threshold.

As long as CTF correction is not routinely applied in electron tomography, the achievable resolution is approximately that of the first zero of the CTF (Table 1), which is higher when imaging at lower defocus. Imaging closer to focus, however, results in images with less contrast for low frequencies, so that identifying and aligning fiducial gold markers or other structures in the tomograms becomes more difficult. A promising way to recover low frequencies is the use of phase plate devices (Nagayama and Danev, 2008) as recently applied for tomography data collection (Murata et al., 2010). An alternative approach used for single particle cryo-EM is the acquisition of pairs of images at different defocus settings, so that complementary high and low frequencies can be recovered from the two images (Ludtke and Chiu, 2003).

In this paper we propose recording two tomographic tilt series of the same object, first at low and then at high defocus, to obtain both high-resolution/low-contrast and high-contrast/low-resolution data, and we here present an approach for numerical treatment that exploits the combination of the two types of data. In particular, we show that alignment parameters computed for the high-defocus tilt series can be exploited to align the corresponding low defocus tilt-series. This approach allowed us to reliably resolve bacterial membranes as phospholipid double-layers for cells thicker than 500 nm. Further, using synthetic data we show that exploiting combined properties of low-defocus and high-defocus particles can increase the resolution attainable by sub-tomogram

Table 1
Resolution of structures derived from sub-tomogram averaging.

Object	Defocus (μm)	First zero of CTF (nm)	Resolution (nm)	Reference
Nuclear pore complex	–12...–15	4.7...5.3	5.8	Beck et al. (2007)
Spirochete flagellar motor	–10...–18	4.3...5.8	7.0	Murphy et al. (2006)
Spirochete flagellar motor	–10	4.3	4.6	Kudryashev et al. (2009)
Spirochete flagellar motor	–4...–6	2.7...3.3	3.5	Liu et al. (2009)
Human 80S ribosome	–6	3.3	3.9	Brandt et al. (2010)
Cadherins in desmosomes	–4	2.7	3.4	Al-Amoudi et al. (2007)
Desmosomal plaque	–4...–9	2.7...4.1	3.2	Al-Amoudi et al. (2011)
OprM–MexA complex, efflux pump	–4	2.7	3.0	Trepout et al. (2010)
SIV envelope spike	–4...–6	2.7...3.3	2.8	Zanetti et al. (2006)
Env protein of murine leukemia virus	–4...–6	2.7...3.3	2.7	Forster et al. (2005)
GAG with point mutations	–2.6...–2.9	2.3	2.7	de Marco et al. (2010)
HIV structural component GAG	–2	1.9	2.1/1.7	Briggs et al. (2009)
HIV-1 gp120 trimer	–2	1.9	2	Liu et al. (2008)

averaging techniques, thus suggesting focal pair tomography as a promising approach towards obtaining higher resolution with cryo-ET.

2. Methods

2.1. Generation of high resolution tomograms

Focal pair tomographic reconstructions were generated using experimental data from two bacterial types as described below. Further, we detail the different algorithmic approaches used to align the low-defocus tilt series in the focal pair setting, and assess the quality of the resulting reconstructions.

2.2. Data collection

For cellular tomography two tomograms were acquired for each imaged bacteria *Yersinia enterocolitica* or *Caulobacter crescentus*: first with underfocus of 2 μm (low defocus) followed by 15 μm (high defocus), using the FEI batch tomography software on an FEI Titan Krios (300 kV accelerating voltage, Cs = 2.8 mm) equipped with a Tridiem Gatan Imaging filter (GIF) and a 2 × 2 k Gatan US1000 post-GIF camera. The total dose used for each tomogram was kept below 10,000 electrons per nm², aiming at an angular coverage of 120° in 41 steps of 3° for thicker bacteria *Y. enterocolitica* and 61 steps of 2° for *C. crescentus* with higher dose applied to higher tilting angles. Pixel sizes for *Yersinia* and *Caulobacter* data were 0.74 and 1.048 nm, respectively.

2.3. Focal pair alignment for large field tomography

Alignment of the high-defocus tilt series was done based on 10 nm fiducial gold markers present in the sample, using the Eto-mo software (Kremer et al., 1996). Fiducial gold alignment was

not possible for most low-defocus tilt series, due to the low contrast of the gold markers especially at high specimen tilt angles. The low-defocus tilt series therefore needed to be aligned with the help of the high-defocus series. We tested different strategies to align the low-defocus series with their high-defocus companions:

2.3.1. Tilt series alignment Method 1: Global alignment by image correlation

Comparison between low- and high-defocus images was performed by cross-correlation of the *entire images*. First, both high- and low-defocus images were band-pass filtered to a resolution range between 32 and 6 nm^{–1} (Fig. S1A). Next, the low-defocus images were aligned to high-defocus images by maximizing cross-correlation, allowing a rotation range of –1.3–1.3° and a maximum translation of one quarter of the image size. The identified optimal alignment parameters between the low-defocus and high-defocus images for shifts and rotations were added to the alignment parameters previously determined for the high-defocus images, to yield the alignment parameters for the low-defocus tilt series.

2.3.2. Tilt series alignment Method 2: Local feature alignment

Alternatively, comparison between low- and high-defocus images was done by cross-correlation between sub-images located around features of interest identified in the high-defocus tomographic reconstructions. This procedure aimed at compensating for potential density movements during tomographic data acquisition. Features of interest (we tested a membrane layer and a bacterial flagellar motor) were picked from tomograms recorded at high defocus. The positions of these features in the high- and low-defocus projections were calculated, and patches of 400 × 400 nm² image size were extracted from the recorded tilt series. The alignment parameters for the high-defocus tilt series were then corrected by the determined cross-correlation offsets (Fig. S1C), allowing a maximum of 5 nm shifts. Feature-pairs with higher shifts between the high- and low-defocus datasets were discarded from further processing. The aligned particles of interest were then reconstructed using the additional shifts from the local alignment.

2.3.3. Tilt series alignment Method 3: Alignment by correlation of fiducials

In order to compensate for fiducial gold movement during tilt series acquisition, we aimed at aligning image patches of low-defocus tilt series containing fiducial gold markers to an idealized gold template. The determined positions of the gold beads in the high-defocus images were used as an initial estimation for the positions in the low-defocus micrographs. Since the gold markers were exposed to irradiation with 10,000 electrons per nm² during each tilt series, they changed their physical positions in the ice layer (Fig. S1E). Operationally, gold marker positions from high-defocus tilt series were exported to the low-defocus tilt series, and used as seed to perform local cross correlation searches for best fits to a gold marker, allowing a maximum shift of 10 nm over the entire tilt series. The low defocus reconstructions were calculated using the refined positions of the gold markers by regular fiducial alignment (Amat et al., 2010b). Note that this method differs conceptually from Method 2 (local feature alignment). The set of marker positions identified by Method 3, alignment by correlation of fiducials, is used for the reconstruction of the whole tomogram, while positions identified in Method 2 provide local reconstructions for each analyzed feature.

2.3.4. Tilt series alignment Method 4: Fiducial marker alignment of low-defocus tilt series

We also tried to directly align the low-defocus tilt series images with each other and without referring to the high-defocus series. The most straightforward approach is the use of gold beads as fiducial markers. As mentioned above, this failed for most of the tilt series due to low image contrast especially at high tilting angles, except for very few cases.

2.3.5. Tilt series alignment Method 5: Markerless alignment of low-defocus tilt series

Regular cases, where gold beads are in practice invisible, may be addressed with markerless alignment methods (Castaño-Díez et al., 2007; Sorzano et al., 2009; Winkler and Taylor, 2006). Here, we used Alligator (Castaño-Díez et al., 2010), which performs an exhaustive analysis of the tilt series looking for local image areas that can be recognized across different projections, and whose centers can thus function as fiducial markers.

In both cases, with or without fiducials, as the reconstruction of low- and high-defocus datasets proceeded independently, locating equivalent spatial positions in high- and low-defocus tomograms required registering them by cross correlation.

Reconstructions were performed by weighted back projection using Imod (Kremer et al., 1996), the Tom package (Nickell et al., 2005), and own custom programs written in MATLAB.

2.4. Tomogram quality evaluation by “bilayer analysis”

In order to evaluate the quality of the obtained 3D reconstructions, we developed a method to average 2D lipid bilayer patches that were abundantly present in the tomograms. We compared the four methods of focal pair alignment for tomogram generation in respect to their ability to produce a well-resolved lipid bilayer.

Imaged bacteria (or specific locations of the bacteria for the tilt series alignment Method 2) were 3D reconstructed with the five different focal pair tomography alignment methods described above. For this analysis we used a tomogram of 500 nm thick *Y. enterocolitica* which we could align using fiducial gold markers (Method 4). Slabs of 22 nm thickness were then manually cropped from the reconstructed volumes, so that the bacterial membranes in these slabs were oriented perpendicular to the slab surfaces. These slabs were then vertically projected into 2D images, which showed the bacterial membranes as curved lines. From these projection images, 450–500 patches of $100 \times 100 \text{ nm}^2$ size were boxed along the membrane lines. The patches were extracted at exactly the same locations from high-defocus and low-defocus reconstructions for tomograms generated by methods 1 and 2, while for methods 3, 4 and 5 we extracted the patches at positions that were corresponding to each other. These patches were translationally and rotationally aligned to a straight line of 1.5 nm thickness as an initial template. The average was translationally averaged along the direction of the membrane, which was also used as a reflexion axis for a further mirror-symmetrization. The resulting symmetrized average was used as a reference for a new alignment, repeating this procedure for 40 further iterations.

2.5. Focal pair alignment for sub-volume averaging

Next, we generated synthetic data sets of test volumes with simulated resolution anisotropy and various levels of noise. These data sets were used to analyze the performance of different sub-volume averaging procedures in respect to the processing of focal pair data.

2.6. Construction of synthetic datasets

From a solution structure of *E. coli* 70S ribosome (EMD-1003, Gabashvili et al., 2000) we generated a density map with a pixel size of 1.05 nm and used this to simulate tomographic tilt series datasets and tomographic reconstructions. 300 randomly oriented ribosome volumes were each projected into multiple directions rotated around a vertical tilting axis at angles from -60 to $+60$ with an angular step of 3° , resulting in 41 projection images each. The generated projections were Fourier transformed, and different amounts of white noise were added. The resulting noisy Fourier transforms were multiplied by a CTF of a 300 kV microscope ($C_s = 2.8 \text{ mm}$) operated at $-15 \mu\text{m}$ (‘high’ defocus), -6 or $-8 \mu\text{m}$ (‘medium’ defocus), or $-2 \mu\text{m}$ (‘low’ defocus), and the resulting data were back-transformed into real-space images. The amounts of noise were chosen such that the resulting images had a signal to noise ratio between 1:1 and 1:6 (Fig. 4A), and one noise-free set of images was created, resulting in 7 different noise levels (0–6). For medium-defocus particles, a doubling of the electron dose was simulated by suppressing the noise levels by a factor of 1.412 ($=\sqrt{2}$). We reconstructed each separate ribosome volume for every noise level and CTF modulation to a $40 \times 40 \times 40 \text{ pix}^3$ volume by weighted back projection. As a result of this procedure, 300 ribosome volumes were generated at 7 noise-levels and four defocus sets (MD I, MD II, LD, HD), resulting in $300 \times 7 \times 4 = 8400$ volumes.

These generated volumes were re-combined into fivefour test datasets, to test the performance of the alignment algorithms via sub-volume averaging and feature visibility evaluation. This recombination was done with the following four methods:

- (1) Particles from simulated high-defocus (HD) and low-defocus (LD) volumes without projection misalignment were used separately (7×300 HD and 7×300 LD volumes).
- (2) The simulated focal pair volumes for HD and LD without projection misalignment were merged. For this, the high-defocus volumes were low-pass-filtered to the first zero of the CTF (6 nm) and added to the low-defocus volumes multiplied by 2.7. This coefficient is a ratio of CTF amplitudes at $-2 \mu\text{m}$ and $-15 \mu\text{m}$ over the resolution range from infinity to 6 nm^{-1} resolution (Fig. 1A, graph). This resulted in 7×300 volumes.
- (3) The simulated medium-defocus particle images at under-focus values of $6 \mu\text{m}$ (MD I) and $8 \mu\text{m}$ (MD II) were used without projection misalignment to generate two sets of 7×300 volumes.
- (4) Prior to 3D reconstruction, the simulated HD and LD particle projection images were randomly misaligned by x and y shifts for a maximum of 1 pixel in both directions so that corresponding HD and LD particles were misaligned simultaneously. The low defocus images were then subjected to a further random shift up to 1 pixel in both directions. These mis-aligned particle images were then used for independent 3D reconstructions, resulting in 7×300 HD and 7×300 LD 3D reconstructions. Due to the misalignment of the images before 3D reconstruction, these reconstructed volumes had a slightly degraded resolution.
- (5) A further set of misaligned particles was constructed integrating geometric constraints modeled after the results of the tilt series alignment experiments. To this end, the same steps as in (4) were performed with the following difference: the additional shifts imposed onto the LD particles were in this case not randomly oriented as in (4), but they were defined systematically for all the projections of the same simulated particle, as suggested by the trend found in Fig. S2. Shifts were also imposed similar

to the distribution in Fig. S1D: One third of the particles was displaced by $r = 1$ pixels, another third by $r = 2$ pixels, and the last third by $r = 3$ pixels.

2.7. Alignment and averaging procedures for simulated datasets

To simulate sub-volume alignment and averaging, the four datasets of volumes created above were used. Three different approaches of alignment and averaging were tested. Each approach represented a higher level of integration of low and high frequency information. At all steps a spacious spherical mask with Gaussian smoothed edges was used; particles and references were low-pass filtered to the first zero of the applied CTF.

2.7.1. Volume alignment Method 1: Iterative refinement

In this alignment procedure, the particles were iteratively 3D aligned to a reference and averaged. A ribosome volume low-pass filtered to 15 nm resolution was used as a starting reference. Iterative refinement was done for 150 rounds, in each of which the assigned orientations were refined through a search over a cone with a random angle, followed by global translational correlation search, while optimizing normalized, wedge-compensated cross correlation between the sub-volumes and the current reference volume. After alignment, in each iteration all particles were averaged to produce the next reference structure. This approach was used for all datasets.

2.7.2. Volume alignment Method 2: Particle replacement

In this alignment procedure, alignment parameters from an iterative alignment as described above for the high-defocus particles alone were used to generate an average from the corresponding low-defocus particles. This approach was only applied for particles that had focal pairs, i.e. the datasets 1 and 4.

2.7.3. Volume alignment Method 3: Replacement and refinement

This sub-volume alignment procedure represents the idea of focal pairing: the alignment parameters determined for the high-defocus particles of a focal pair dataset were used as starting parameters for a local alignment refinement with the low-defocus particles. The refinement search was restricted to only small shifts (maximum of 3 nm) and limited angular variations. This procedure was only performed for 10 iterations, whereby in the first eight iterations of sub-volume alignment, a local orientation search over an angular range of $\pm 5^\circ$ between the HD and LD alignment parameters was allowed, and in the following 2 iterations only a refinement search over a range of $\pm 2^\circ$ was allowed. Also this approach was only applied for particles that had focal pairs, i.e. the datasets 1 and 4.

This alignment method has been devised because pure replacement of alignment parameters computed with low frequency information under noisy conditions (as delivered by Volume Alignment Method 2) is not expected to yield and accurate alignment for high frequency components. This effect has been explored for a simplified situation in Fig. S3.

In all cases, an in-house modified version of the AV3 package for MATLAB (Forster et al., 2005; Kudryashev et al., 2009) was used for the processing.

3. Results

3.1. Generation of high-resolution tomograms

In order to establish the processing methodology we acquired first low- and then high-defocus tilt series from two types of bacterial cells: 400–500 nm thick *C. crescentus* and 500–700 nm thick *Y. enterocolitica*. We used 2 μm underfocus (low defocus, 'LD'),

yielding the first zero of the CTF at $\sim 2 \text{ nm}^{-1}$ for high resolution imaging, and 15 μm (high defocus, 'HD'), yielding the first zero of the CTF at $\sim 6 \text{ nm}^{-1}$ (Fig. 1A) for high contrast imaging for low frequencies (Fig. 1B, left). The pixel size used for *Yersinia* was 0.74 nm, at which the first zero of the CTF was still within the theoretical sampling limit of 1.48 nm^{-1} resolution.

Misalignments during tilt series registration seriously degrade the resolution of the final 3D reconstruction. We thus tested five alignment methods: The first three methods register images of low-defocus tilt series to the corresponding high defocus images and use alignment parameters of high defocus tilt series to generate a reconstruction (see more in Section 2): Method (1) performs global alignment of low- and high-defocus tilt series; Method (2) does a refinement of alignment parameters by local features that typically modified the position of a global alignment by a few nanometers (Fig. S1D) in a direction that was consistent for each feature over the range of tilt images (Fig. S2); Method (3) refined the alignment parameters by fiducial gold markers. The last two methods perform an independent alignment of low- and high-defocus tomograms. Method (4) implied the use of gold beads, the method of choice. and method (5) implied the use of markerless-alignment methods. These were often required, when low-defocus tomograms had too low contrast for a fiducial gold marker-based reconstruction. While high-defocus reconstructions showed strong contrast and clearly revealed large macromolecules inside the cell, low-defocus reconstructions were able to resolve lipid bilayers even with the simple Method 1 (Fig. 1B).

Next, tomogram quality was evaluated using lipid bilayers as abundant features in the tomograms of biological objects like bacteria, cells, and tissues. We focused on one single *Yersinia* cell for this experiment, which was $\sim 550 \text{ nm}$ thick and extracted six sets of membrane patches. Five sets were extracted from five different versions of the low-defocus tomogram, each obtained with a different alignment method in the order described above. We selected one of the few cases, where gold beads were distinguishable, in order to be able to consider a representative of Method 4, based on the presence of gold beads in the low-defocus tilt series. The fifth set involved the use of markerless alignment methods, which is a method that was initially designed for electron tomography datasets without gold beads. To provide representatives of methods 4 and 5 from the same data set, the markerless alignment software Alligator was used, while avoiding image patches that contained gold beads when analyzing the low-defocus projections. The sixth set of membrane patches was extracted from the high-defocus tomogram.

In spite of being initiated with a reference without bilayer features, all tested alignment methods recovered a bilayer-like structure, with different degrees of clarity. A summary of the visual impression of the different bilayers – roughly confirmed by the FRC lines – is as follows: The most simple algorithmic approach, Method 1, showed a fairly distinct bilayer (Fig. 2A, M1) while the more-involved strategy of local image feature alignment yielded an even better defined bilayer (Fig. 2A, M2). Method 3 decreased the quality of the bilayer (Fig. 2A, M3). Best resolved bilayers were recovered, when the alignment was done based on manually selected gold beads from the low defocus tilts series (Fig. 2A, M4). Markerless alignment did also produce a valid bilayer (Fig. 2A, M5). The high-defocus dataset did not produce a recognizable bilayer structure (Fig. 2A, "HD"). Fourier ring correlation showed that methods 2, 4, and 5 performed slightly better than methods 1 and 3; all methods however had a correlation close to 0.5 at the resolution level of 3.75 nm^{-1} (Fig. 2B). Patches of white noise did not produce a bilayer (Fig. 2C).

The intensity profile lines in the right column of Fig. 2 can be interpreted as a quantitative estimation on effective resolution of the tomograms, as they establish an object separation length that can be detected with an adequate data analysis procedure. The

peak-to-peak distance between the resolved dark peaks of the bilayer cross-sections is 3.75 nm in all alignment methods, indicating that the obtained resolution was at least 3.75 nm^{-1} .

3.2. Tolerance to additional electron dose

As the total electron dose for recording both LD and HD tomograms was around $20 \text{ ke}^-/\text{nm}^2$, the lastly acquired images occasionally showed signs of electron damage for the thick *Yersinia* cells. For some focal pair tomograms we applied up to $30 \text{ ke}^-/\text{nm}^2$. In these cases, even though the reconstructions from the later recorded high-defocus images were severely electron damaged (Fig. 3A), the low-defocus tilt series did not show signs of electron damage (Fig. 3B), and the quality of the alignment (by global alignment) was sufficient to be able to resolve lipid bilayers, thus preserving the resolution of the tomogram in the range of $3\text{--}4 \text{ nm}^{-1}$ (Fig. 3C).

3.3. Sub-tomogram alignment of focal pair particles

The algorithmic approach for mutual alignment of sub-tomograms described in the Method sections was systematically applied to five synthetic ribosome datasets, each with various levels of noise: (1) separate high- and low-defocus particles; (2) merged focal pair particles; (3) particles simulated at intermediate defocus; and (4) separate high- and low-defocus particles with projection

misalignment; (5) separate high- and low-defocus particles with directed projection misalignment imitating errors from global alignment of HD and LD tilt series registration (Fig. 4A). The obtained results characterize the performance of the modifications of known numerical methods for the processing of focal pair data at recovering the resolution of the initial template.

The alignment of high defocus particles from dataset (1) reliably converged to the initial structure within the resolution limit of the high-defocus particles at roughly 6 nm^{-1} for the noise levels 1–4 (Fig. 4B, 'HD'). Simple replacement of the high-defocus particles by low-defocus particles while applying the same translations and rotations failed to retrieve the lower frequencies of the initial structure (Fig. 4B), but partially recovered the high frequencies. However, the entire structure could be recovered by local iterative refinement of alignment parameters from the high-defocus datasets with low-defocus particles (replacement + refinement). The local alignment for low-defocus particles from dataset (1) converged for noise levels 0–3 to almost the theoretical sampling limit 2.1 nm^{-1} (Fig. 4B 'LD'). For noise level 4 the correlation with the EMDB structure at high frequencies was lower, indicating worse convergence for this noise level. The replacement and refinement method repeated this trend also when the simulated particles incorporated a realistic level of alignment error (dataset 4). In this case, using the replacement and refinement method made possible the recovery of the structure up to noise level 3 for the LD particles. Alignment of LD particles without the HD information converged

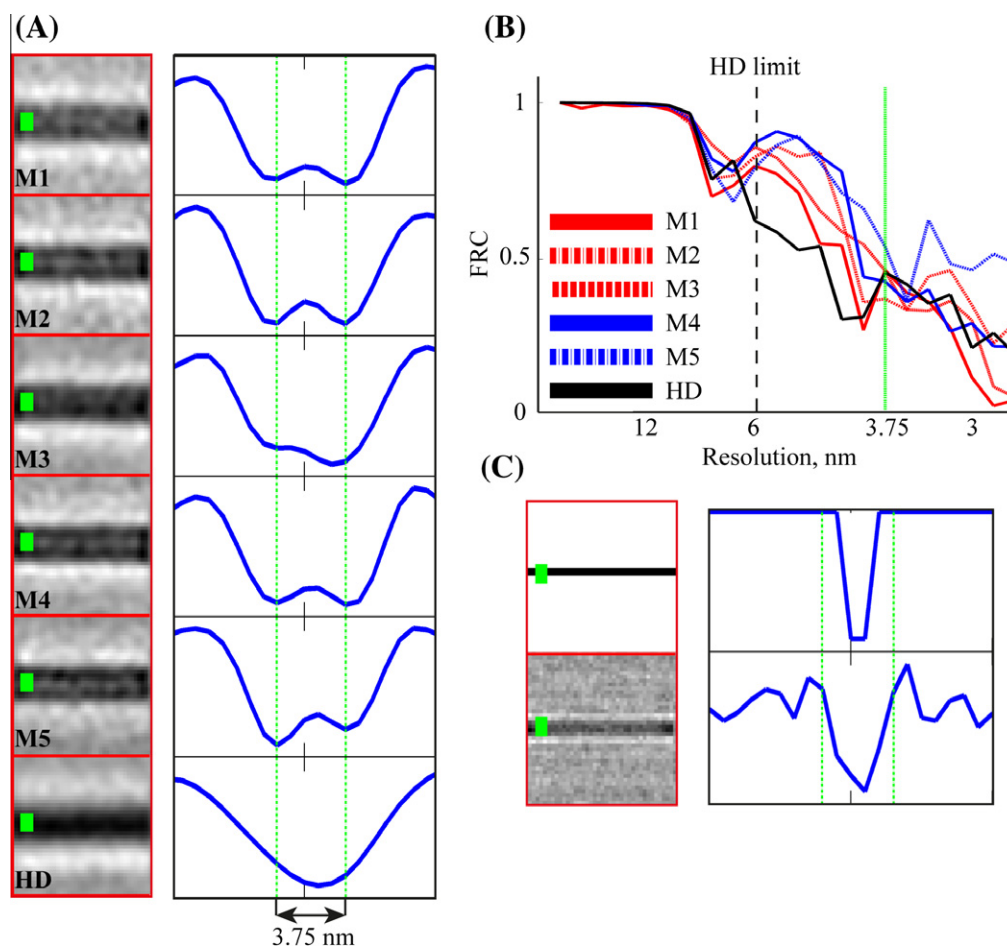


Fig. 2. Bilayer recovery in low defocus tomograms. Left column shows non-symmetrized averages of bilayer fragments resulting from different alignment methods of the low-defocus stack. Row (A) corresponds to alignment by global correlation of images (Method 1), (B) alignment by local correlation of image features (Method 2), (C) alignment by tracking of gold bead templates (Method 3), (D) alignment by manual clicking of gold beads (Method 4), (E) high-defocus data. Right column contains the corresponding intensity profiles across the vertical center line of each bilayer depicted on the left. The distance between the inverse peaks detected by the three most successful methods for alignment of low defocus data (rows A, B, and D) is 5 pixels or 3.75 nm.

to the real structure for noise level 1, if a template pass filtered to 15 nm^{-1} was used, and up to noise level 2, when the template was pass filtered to 6 nm^{-1} .

The second approach for the integration of high- and low-defocus information corresponds to processing of merged particles *ab initio*. Such refinement showed better convergence at lower frequencies – for noise level 5 it agreed with the EMBD structure up to the high-defocus resolution limit (Fig. 4B ‘Merged’). However in the frequency range around $5\text{--}7 \text{ nm}^{-1}$, where the CTF of the high-defocus dataset had its first zero and the CTF of the low-defocus dataset still had low amplitudes, the resolution did not correspond well with the EMBD structure for all the noise levels.

Alignment of medium-defocus particles from dataset (3) simulated at -6 and $-8 \mu\text{m}$ defocus and with twice the applied electron dose converged to the initial structure up to a resolution corresponding to first zero of their CTF from datasets up to noise levels 4 and 5 correspondingly (Fig. 4B, ‘MD’). A summary of the degree of alignment success of the different approaches is presented in Table 2.

4. Discussion

4.1. Tilt series alignment

In order to compare the quality of tomograms at a resolution level of $3\text{--}4 \text{ nm}^{-1}$, we proposed a criterion based on the quality of lipid bilayer recovery in tomograms. This bilayer quality assess-

ment sets the ground for testing and mutual comparison of different algorithmic approaches towards the alignment of low-defocus tilt series paired with their high-defocus companions. Another possible way to assess the quality of tomograms could be template matching in combination with sub-volume averaging followed by structural comparison with known atomic models of the proteins, where available. The resulting resolution could give a quantitative measure of tomogram quality. Our method, however, is free from particle selection bias due to the template matching. The here applied manual selection of membrane patches for averaging is much less prone to artifacts.

We here present a generally applicable method that is able to work on a single 3D reconstruction and does not require extensive calculations. In addition, lipid bilayers are abundant in most biological tomography data, and their approximate locations are easily recognizable both to the human eye and to computer procedures. We believe this method can be used to access the quality of reconstructions at a resolution level of 3 nm^{-1} in whole mount preparations as well as cryo sections and focused ion beam (FIB)-milled preparations (Rigort et al., 2010).

All the alignment methods were able to visually resolve lipid bilayers in tomograms of thick cells (Fig. S1F). The most simple and direct method, i.e. independent alignment of low defocus tilt series by gold markers already produces bilayers of high quality and should probably be the method of choice wherever possible. Unfortunately, in our experience, this strategy cannot be used in every tomogram because of the reduced SNR in thick samples,

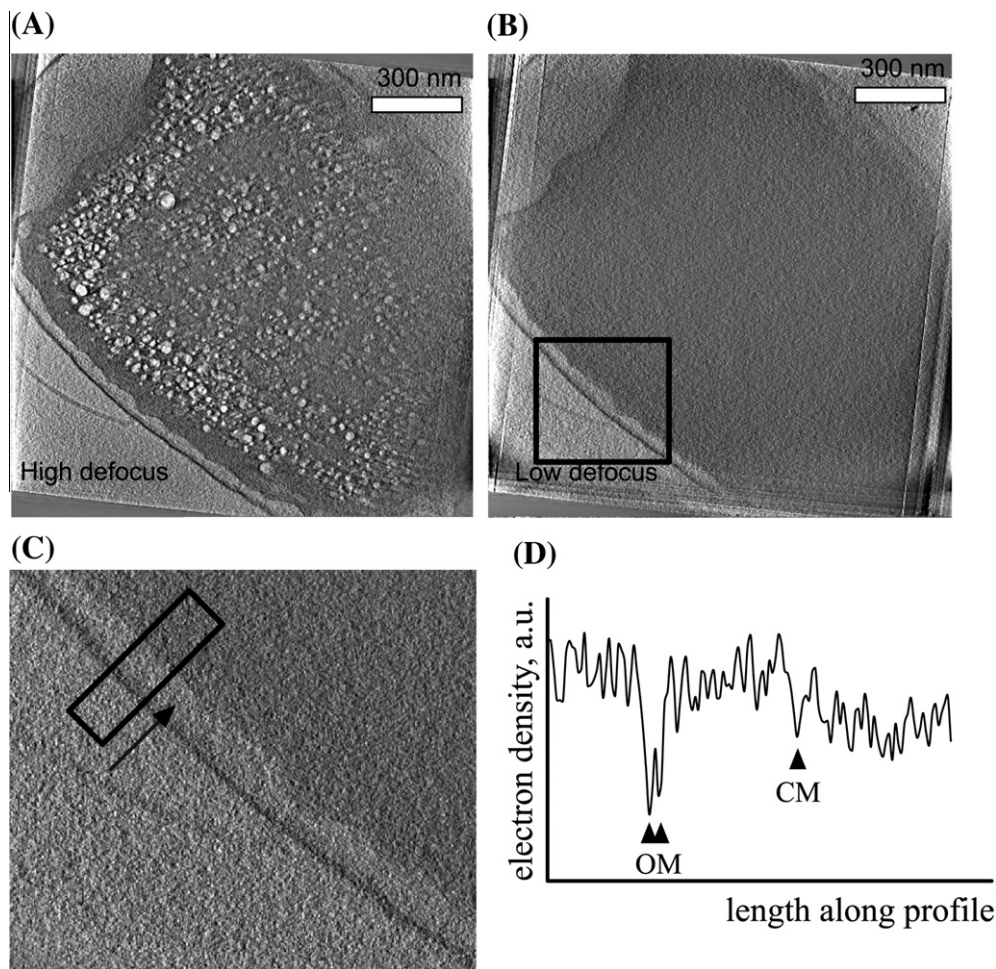


Fig. 3. Higher electron dose applied during focal pair tomography acquisition. (A) A 20 nm thick section through a tomogram of an electron-damaged $\sim 500 \text{ nm}$ thick *Yersinia* cell recorded at high defocus. (B) A 20 nm thick section through a tomogram of the same bacteria as in A acquired before and reconstructed by global alignment ('Method 1'). Scale bars: 300 nm. (C) Inset from B and (D) an electron density profile from a lateral projection of the pixels indicated by the boxed area, showing a lipid bilayer resolved.

Table 2
Performance of the three methods of sub-tomogram averaging on the five synthetic ribosome datasets. Shown is the attainable resolution and the noise level, at which the resolution was reached.

Dataset	Refinement		Particle replacement		Post replacement refinement		
		CTF limit (nm)	Best noise level	CTF limit (nm)	Best noise level	CTF limit (nm)	Best noise level
1. Separate focal pairs	HD	6	4	2	0	2	4
	LD	2	1				
2. Merged FP		2	4	N/A		N/A	
3. Intermediate defocus	6 μm	3.3	4	N/A		N/A	
	8 μm	3.9	5				
4. Misaligned FP	HD	6	3	2	0	2	3
	LD	2	1				
5. Systematically misaligned FP	LD	2	1	2	0	2	3

especially at high tilting angles, i.e. at 60° where the effective thickness of the ice layer increases twofold. At the cost of increased user intervention, one markerless alignment technique was able to produce bilayers of similar quality in our experiments. In the general case, however, markerless alignment procedures should be used with caution when analyzing thick, ice embedded specimens, and they are not widely used as replacement for gold bead based alignment of single tilt series.

For this reason, we have presented and explored other possible approaches that apply the same principle of cross-correlation, adapted to the scenario of focal pair tomography. A fundamental difference is that the duplicated image recording of the same scene allows focal pair tomography to infer the alignment parameters from direct comparison of images of the same tilt angle, representing thus the same scene, although with different modulation of frequency components. Markerless alignment methods instead operate by comparing images of different tilt angles, or images with computational reprojections of reconstructed models. Both cases perform better with smaller angle increments between two consecutive tilts, a constraint that does not apply when comparing focal-paired tilts. Further, in an approach based purely on cross correlation the alignment of a sample whose dynamics deviates from the rigid body model during data acquisition is not trivial, as it requires disentangling false positives of cross-correlation from genuine inhomogeneous movements in the sample. In the focal pair tomography setting, coping with such cases would imply using the location of the gold beads in HD, which are objectively defined, to characterize coarsely the dynamics of the sample.

Among these specifically tailored procedures, we found simple global alignment of the LD tilt series to the pre-aligned HD to be a reliable and numerically stable method to generate a LD tomogram. It implies minimal user intervention, does not require any controls, and produces reconstructions with bilayers of good quality. Local refinement according to local features improves the quality of reconstructions compared to global alignment. We interpret this improvement as the success of the method in compensating the effect of anisotropic density movements in the sample during the acquisition of the tilt series. The displacement of density depends on the applied electron dose and in our case followed a Poisson distribution with the probability peak at 2 nm (Fig. S1D). Interestingly, the direction of displacement was consistent over the range of tilting angles, indicating that density movement happens smoothly in one direction during electron exposure. Positions that were close to each other also moved into similar directions (Fig. S2) suggesting that density movement has also a large scale movement component. Similar directionality of the displacement was true also when the positions marked in Fig. S2 were refined with the size of the patch of 150 nm.

Local refinement around gold beads reduced the average quality of the bilayer; the most likely reason is that the center of the gold bead in the low dose projection micrographs was not always corresponding to the center of the bead template; other contrast

features like membranes could have also interfered with the alignment process. At its current state, we would not recommend using this method. However, more advanced feature tracking algorithms in combination with geometrical information could turn such refinement into a viable strategy.

4.2. Resolution gain in sub-tomogram averaging

We picture that focal pair tomography can readily be used for cell-biological applications, i.e. detecting membrane topologies or the periodicity of filaments inside cells in order to identify the characteristic patterns known from single-particle cryo-EM. We further focused on the adaptation of focal pair tomography for sub-tomogram averaging. On the basis of well-established numerical algorithms we have described slight procedural modifications adjusted for the optimal integration of high- and low-defocus data. Our simulations show that in the presence of noise, simple alignment of high-defocus particles and replacing particles to the corresponding low-defocus particles does not result in a reliable resolution gain (Fig. 4B), and the alignment parameters have to be locally refined. The reason can be tracked down to the interplay of frequency content and the ability of cross correlation to align accurately structures of fine detail in presence of noise. When sampling the parameter space for comparing by cross correlation a template against noisy data, fine structures produce sharp peaks of accurately defined maxima, while coarse structures produce wider peaks. In numerical terms, given a set of positions and angular orientations that is sufficient to align the data to low resolution, a different set of parameters that is close enough to the optimal set will still produce an average of similarly low resolution for noisy data, and might fail to satisfactorily align the high frequencies.

We illustrate this intuitive effect in Fig. S3, which aims to depict the different qualitative behavior of HD and LD data in the framework of cross correlation-based alignment from the numerical point of view. It considers two templates of a ribosome, each one pass-filtered to a different frequency range, and explores, to which accuracy translational and rotational alignment can recover the exact position and orientation of the bandpassed template in copies of itself affected by noise of increasing strength. The most evident feature in this figure is that cross correlation maxima extend over a wider angular range for HD data. This translates into the very intuitive fact that the cross correlation maxima will be sharper defined when aligning high frequency structures: small rotations can generate a full mismatch of fine details between the template and the copy. As a result of this, we observe the second feature: noise degrades the numerical accuracy of the alignment, as the location of the cross correlation peak wanders off from the real angular position. For equivalent levels of noise, the measured error is higher for the wider high defocus peaks. These two qualitative observations are the basic ground for the interplay between high and low frequencies suggested in the algorithm.

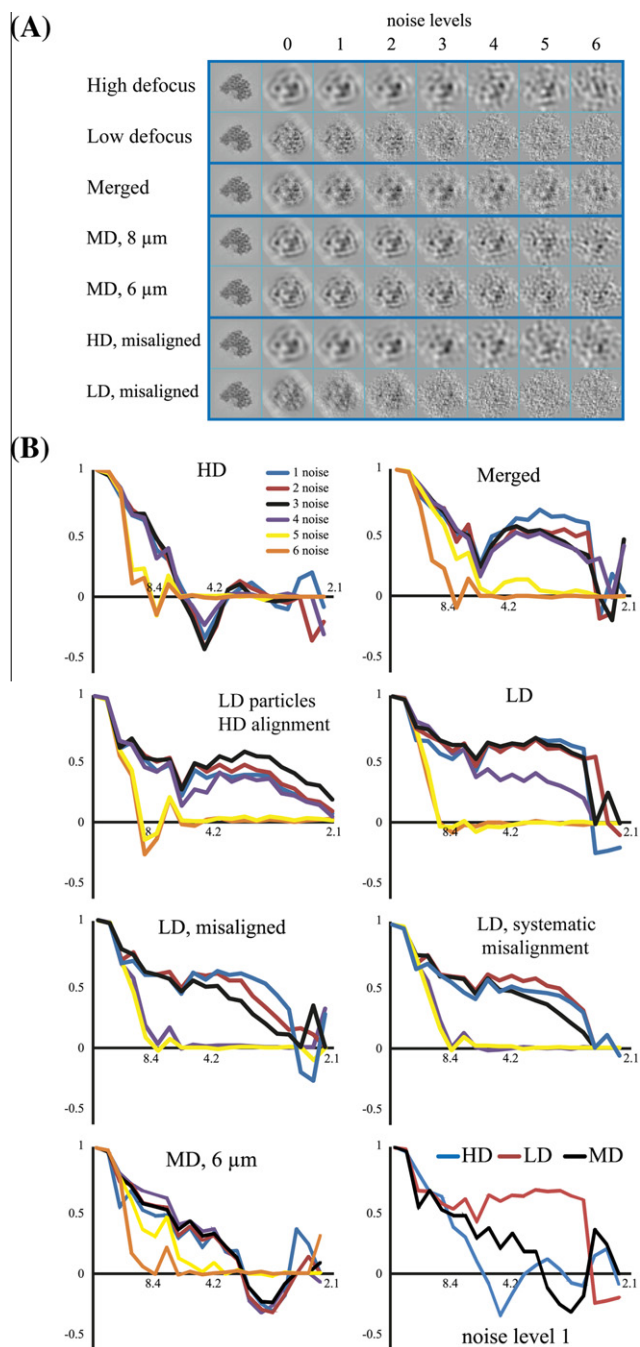


Fig. 4. Tomographic sub-volume averaging of *in silico* generated ribosome datasets. (A) Example particle images of the created ribosome test data in the same orientation at different levels of underfocus and noise. The first column shows the projected atomic ribosome structure. The following columns show the projection images at noise levels 0–6 (see Section 2). (B) FRC (Fourier Ring Correlation) curves between average structures and the initial EMDB structure for different noise levels for different particle sets. HD: high-defocus alignment, LD: low-defocus alignment, originating from high-defocus alignment (see Section 2); Merged: alignment of merged particles; LD, misaligned: alignment of low-defocus particles starting from alignment of high-defocus particles for the misaligned dataset; MD: particles simulated with underfocus of 6 μm with twice the electron dose; bottom right: comparison of resulting resolution curves for HD, MD and LD at noise level 1.

The tested approaches are successful at exploiting the combination of information of different frequency contents, as they manage to extract a better balance between the resolution attained by the recovered structures and the strength of the noise imposed onto the dataset. Different levels of noise were used in order to model

image degradation caused by limited electron dose, varying cell thickness, instrumental distortions, etc.

Comparable results were attained by the two numerical approaches explored in this work: post replacement refinement (successive alignment of HD and LD particles) and merged refinement (alignment of particles constructed by systematic merging of HD and LD particles). Although qualitatively similar, each method presents slight advantages over the other: while merged refinement can be successfully operated for slightly higher levels of noise, replacement refinement recovers the original signal in a more uniform manner along the frequency range. The use of merged particles requires amplitude correction of the CTF components for both HD and LD images. This requires a quantitative image formation description for the experimental data. On thick cells, a reliable description of the imaging process is a difficulty shared with methodologies oriented to the numerical correction of the CTF. Replacement refinement, on the contrary, does not need any estimation on CTF parameters, an advantage that showcases it as a robust computational framework.

Importantly, our simulations demonstrate that having high-defocus information improves the initial convergence: high-defocus particles converge to the real structure at noise levels up to 4, while only low-defocus particles converge only up to noise level 1. Convergence of particles simulated at intermediate defocus is slightly better (up to noise level 5 for 8 μm underfocus). However, they converge only up to a CTF-limited resolution of roughly 4 nm⁻¹, while the CTF limit for low-defocus particles is 2 nm⁻¹. Thus, focal pair tomography in combination with sub-tomogram averaging provides a better convergence/resolution ratio.

It is worth mentioning that template matching, a framework for visual proteomics, uses the same algorithmic approach by finding a mutual orientation of a fully sampled reference with a high signal to noise ratio to a low signal to noise part of a tomogram with the missing wedge (Frangakis et al., 2002). Thus focal pair tomography can be useful for template matching in order to minimize the template bias using both high- and low-resolution/contrast information. Focal pair tomography also contains a capability of internal cross validation: since LD and HD tomograms have different noise properties, it is possible to pick particles in HD or merged tomograms and then check if high frequencies of the reference correspond to high frequencies of the LD particles.

4.3. Data acquisition protocols

Considerations about the electron beam-induced sample damage are especially relevant in focal pair tomography, where the total electron dose has to be divided on two different tilt-series collected on the same sample. Preservation of high frequencies calls for acquiring first the full tilt series in low-defocus conditions. We show that if the high-defocus tilt series collected afterwards shows signs of severe beam damage, it is still possible to recover high-resolution information “before damage”. This allows applying slightly higher electron dose without the risk to damage the fine structure of the object. Our suggestion, however, is to pick the objects not directly affected by electron damage for analysis like the flagellar motor from Fig. 3A. Such acquisition scheme may be performed on every microscope with standard acquisition routines, doubling the microscopy time required for data acquisition. This however could be accelerated by the implementation of automated tomographic acquisition software that uses information stored during the collection of the low-defocus tilt series for tracking during high defocus tilt series acquisition.

Another way to acquire focal pair tomograms is the coupled acquisition of low- and high-defocus images for every tilt angle. This does not allow applying higher electron dose but avoids misalignments due to stage or severe specimen movement between

the corresponding images. This scheme has been implemented in the latest version of EM-Tools acquisition software for TVIPS cameras (<http://tvips.com/>).

In both acquisition schemes, doubling the number of low-dose micrographs multiplies the detector noise by a factor of 2. This specific need to limit detector noise favors collecting tilt series with high angular increments, and makes the future development and introduction of direct electron detectors especially beneficial in the context of focal pair tomography.

Acknowledgments

We thank the groups of Guy Cornelis and Urs Jenal for providing bacteria used for imaging, Bill Anderson, Kenneth Goldie, and Radosav Pantelic for help with microscopy, discussions and comments on the manuscript, and Ilya Yakovlev, Fernando Amat for discussions and comments on the manuscript. The work was supported by the CINA grant from SystemX.ch, the Swiss Initiative for Systems Biology, and by the Swiss National Science Foundation NCCRs Nano, TransCure, and Structural Biology.

Appendix A. Supplementary data

Supplementary data associated with this article can be found, in the online version, at [doi:10.1016/j.jsb.2011.10.004](https://doi.org/10.1016/j.jsb.2011.10.004).

References

- Al-Amoudi, A., Díez, D.C., Betts, M.J., Frangakis, A.S., 2007. The molecular architecture of cadherins in native epidermal desmosomes. *Nature* 450, 832–837.
- Al-Amoudi, A., Castaño-Díez, D., Devos, D.P., Russell, R.B., Johnson, G.T., Frangakis, A.S., 2011. The three-dimensional molecular structure of the desmosomal plaque. *Proc. Natl Acad. Sci. USA* 108, 6480–6485.
- Amat, F., Comolli, L.R., Moussavi, F., Smit, J., Downing, K.H., Horowitz, M., 2010a. Subtomogram alignment by adaptive Fourier coefficient thresholding. *J. Struct. Biol.* 171, 332–344.
- Amat, F., Castaño-Díez, D., Lawrence, A., Moussavi, F., Winkler, H., Horowitz, M., 2010b. Alignment of cryo-electron tomography datasets. *Methods Enzymol.* 482, 343–367.
- Beck, M., Lucic, V., Forster, F., Baumeister, W., Medalia, O., 2007. Snapshots of nuclear pore complexes in action captured by cryo-electron tomography. *Nature* 449, 611–615.
- Beck, M., Malmstrom, J.A., Lange, V., Schmidt, A., Deutsch, E.W., Aebbersold, R., 2009. Visual proteomics of the human pathogen *Leptospira interrogans*. *Nat. Methods* 6, 817–823.
- Brandt, F., Carlson, L.A., Hartl, F.U., Baumeister, W., Grunewald, K., 2010. The three-dimensional organization of polyribosomes in intact human cells. *Mol. Cell* 39, 560–569.
- Briggs, J.A., Riches, J.D., Glass, B., Bartonova, V., Zanetti, G., Krausslich, H.G., 2009. Structure and assembly of immature HIV. *Proc. Natl Acad. Sci. USA* 106, 11090–11095.
- Castaño-Díez, D., Al-Amoudi, A., Glynn, A.M., Seybert, A., Frangakis, A.S., 2007. Fiducial-less alignment of cryo-sections. *J. Struct. Biol.* 159, 413–423.
- Castaño-Díez, D., Scheffer, M., Al-Amoudi, A., Frangakis, A.S., 2010. Alignator: a GPU powered software package for robust fiducial-less alignment of cryo tilt-series. *J. Struct. Biol.* 170, 117–126.
- Chen, S., Beeby, M., Murphy, G.E., Leadbetter, J.R., Hendrixson, D.R., Briegel, A., Li, Z., Shi, J., Tocheva, E.I., Muller, A., Dobro, M.J., Jensen, G.J., 2011. Structural diversity of bacterial flagellar motors. *EMBO J.*
- Crowther, R.A., Klug, A., 1971. ART and science or conditions for three-dimensional reconstruction from electron microscope images. *J. Theor. Biol.* 32, 199–203.
- de Marco, A., Muller, B., Glass, B., Riches, J.D., Krausslich, H.G., Briggs, J.A., 2010. Structural analysis of HIV-1 maturation using cryo-electron tomography. *PLoS Pathog.* 6, e1001215.
- Faruqi, A.R., McMullan, G., 2011. Electronic detectors for electron microscopy. *Q. Rev. Biophys.* 44, 357–390.
- Fernandez, J.J., Li, S., Crowther, R.A., 2006. CTF determination and correction in electron cryotomography. *Ultramicroscopy* 106, 587–596.
- Forster, F., Medalia, O., Zauberman, N., Baumeister, W., Fass, D., 2005. Retrovirus envelope protein complex structure in situ studied by cryo-electron tomography. *Proc. Natl. Acad. Sci. USA* 102, 4729–4734.
- Frangakis, A.S., Bohm, J., Forster, F., Nickell, S., Nicastro, D., Typke, D., Hegerl, R., Baumeister, W., 2002. Identification of macromolecular complexes in cryoelectron tomograms of phantom cells. *Proc. Natl Acad. Sci. USA* 99, 14153–14158.
- Frank, J., 2009. Single-particle reconstruction of biological macromolecules in electron microscopy – 30 years. *Q. Rev. Biophys.* 42, 139–158.
- Gabashvili, I.S., Agrawal, R.K., Spahn, C.M., Grassucci, R.A., Svergun, D.I., Frank, J., Penczek, P., 2000. Solution structure of the *E. coli* 70S ribosome at 11.5 Å resolution. *Cell* 100, 537–549.
- Grigorieff, N., 2000. Resolution measurement in structures derived from single particles. *Acta Crystallographica, Section D. Biol. Crystallogr.* 56, 1270–1277.
- Henderson, R., Baldwin, J.M., Ceska, T.A., Zemlin, F., Beckmann, E., Downing, K.H., 1990. Model for the structure of bacteriorhodopsin based on high-resolution electron cryo-microscopy. *J. Mol. Biol.* 213, 899–929.
- Kremer, J.R., Mastronarde, D.N., McIntosh, J.R., 1996. Computer visualization of three-dimensional image data using IMOD. *J. Struct. Biol.* 116, 71–76.
- Kudryashev, M., Cyrklaff, M., Wallich, R., Baumeister, W., Frischknecht, F., 2009. Distinct in situ structures of the *Borrelia burgdorferi* motor. *J. Struct. Biol.*
- Leis, A., Rockel, B., Andrees, L., Baumeister, W., 2008. Visualizing cells at the nanoscale. *Trends Biochem. Sci.*
- Liu, J., Bartesaghi, A., Borgnia, M.J., Sapiro, G., Subramaniam, S., 2008. Molecular architecture of native HIV-1 gp120 trimers. *Nature* 455, 109–113.
- Liu, J., Lin, T., Botkin, D.J., McCrum, E., Winkler, H., Norris, S.J., 2009. Intact flagellar motor of *Borrelia burgdorferi* revealed by cryo-electron tomography: evidence for stator ring curvature and rotor/C-ring assembly flexion. *J. Bacteriol.* 191, 5026–5036.
- Ludtke, S.J., Chiu, W., 2003. Focal pair merging for contrast enhancement of single particles. *J. Struct. Biol.* 144, 73–78.
- Murata, K., Liu, X., Danev, R., Jakana, J., Schmid, M.F., King, J., Nagayama, K., Chiu, W., 2010. Zernike phase contrast cryo-electron microscopy and tomography for structure determination at nanometer and subnanometer resolutions. *Structure* 18, 903–912.
- Murphy, G.E., Leadbetter, J.R., Jensen, G.J., 2006. In situ structure of the complete *Treponema primitia* flagellar motor. *Nature* 442, 1062–1064.
- Nagayama, K., Danev, R., 2008. Phase contrast electron microscopy: development of thin-film phase plates and biological applications. *Philos. Trans. R. Soc. B-Biol. Sci.* 363, 2153–2162.
- Nickell, S., Forster, F., Linaroudis, A., Net, W.D., Beck, F., Hegerl, R., Baumeister, W., Plitzko, J.M., 2005. TOM software toolbox: acquisition and analysis for electron tomography. *J. Struct. Biol.* 149, 227–234.
- Ortiz, J.O., Brandt, F., Matias, V.R., Sennels, L., Rappasilber, J., Scheres, S.H., Eibauer, M., Hartl, F.U., Baumeister, W., 2010. Structure of hibernating ribosomes studied by cryoelectron tomography in vitro and in situ. *J. Cell Biol.* 190, 613–621.
- Patla, I., Volberg, T., Elad, N., Hirschfeld-Warneken, V., Grashoff, C., Fassler, R., Spatz, J.P., Geiger, B., Medalia, O., 2010. Dissecting the molecular architecture of integrin adhesion sites by cryo-electron tomography. *Nat. Cell Biol.* 12, 909–915.
- Philippens, A., Engel, H.A., Engel, A., 2007. The contrast-imaging function for tilted specimens. *Ultramicroscopy* 107, 202–212.
- Rigort, A., Bauerlein, F.J., Leis, A., Gruska, M., Hoffmann, C., Laugks, T., Bohm, U., Eibauer, M., Gnaegi, H., Baumeister, W., Plitzko, J.M., 2010. Micromachining tools and correlative approaches for cellular cryo-electron tomography. *J. Struct. Biol.* 172, 169–179.
- Scherzer, O., 1948. Ein Elektronenoptischer Apochromat. *Zeitschrift Fur Naturforschung Section a-a. J. Phys. Sci.* 3, 544–545.
- Sorzano, C.O., Messaoudi, C., Eibauer, M., Bilbao-Castro, J.R., Hegerl, R., Nickell, S., Marco, S., Carazo, J.M., 2009. Marker-free image registration of electron tomography tilt-series. *BMC Bioinf.* 10, 124.
- Thon, F., 1971. High resolution microscopy using special apertures and phase plates. *J. Electron Microscop.* 20, 215.
- Trepout, S., Taveau, J.C., Benabdelhak, H., Granier, T., Ducruix, A., Frangakis, A.S., Lambert, O., 2010. Structure of reconstituted bacterial membrane efflux pump by cryo-electron tomography. *Biochim. Biophys. Acta* 1798, 1953–1960.
- Urban, E., Jacob, S., Nemethova, M., Resch, G.P., Small, J.V., 2010. Electron tomography reveals unbranched networks of actin filaments in lamellipodia. *Nat. Cell Biol.* 12, 429–435.
- Wade, R.H., 1992. A Brief Look at Imaging and Contrast Transfer. *Ultramicroscopy* 46, 145–156.
- Winkler, H., 2007. 3D reconstruction and processing of volumetric data in cryo-electron tomography. *J. Struct. Biol.* 157, 126–137.
- Winkler, H., Taylor, K.A., 2006. Accurate marker-free alignment with simultaneous geometry determination and reconstruction of tilt series in electron tomography. *Ultramicroscopy* 106, 240–254.
- Xiong, Q., Morphew, M.K., Schwartz, C.L., Hoenger, A.H., Mastronarde, D.N., 2009. CTF determination and correction for low dose tomographic tilt series. *J. Struct. Biol.* 168, 378–387.
- Zanetti, G., Briggs, J.A., Grunewald, K., Sattentau, Q.J., Fuller, S.D., 2006. Cryo-electron tomographic structure of an immunodeficiency virus envelope complex in situ. *PLoS Pathog.* 2, e83.
- Zanetti, G., Riches, J.D., Fuller, S.D., Briggs, J.A., 2009. Contrast transfer function correction applied to cryo-electron tomography and sub-tomogram averaging. *J. Struct. Biol.* 168, 305–312.